Natural Hazards (2020) 102:909–937
https://doi.org/10.1007/s11069-020-03939-4

ORIGINAL PAPER

Assessment of tectonic-controlled rock fall processes threatening the ancient Appia route at the Aurunci Mountain pass (central Italy)

E. Di Luzio[1] · **P. Mazzanti**[2] · **A. Brunetti**[2] · **M. Baleani**[2]

Received: 15 January 2019 / Accepted: 17 April 2020 / Published online: 30 April 2020

Abstract
This research addresses ongoing rock fall processes that affect the tract of the ancient Appia route crossing the Apennines at the Aurunci Mountain pass (central Italy). Elements of cultural heritage are endangered as calcareous blocks descending from the rock slope that delimits the route track were observed lying on the pavement. Based on cooperation between geologists and experts in remote sensing, a multi-disciplinary study was pursued to assess rock fall susceptibility. This study included aero-photogrammetric reconstruction of slope topography, field-based structural and kinematic analyses, terrestrial laser scanner and unmanned aerial system surveys and probabilistic rock fall modelling. This last was performed by simulating a large number of 3D trajectories and initially adopting a lumped mass approach, therefore tracking dimensionless rock blocks (kinematic modelling). The structural setting of the investigated rock slope shows evidence of four tectonic phases, including in chronological order folding, thrusting, strike-slip and normal faulting. Non-homogeneous joint sets distribution within the rock masses, due to the tectonic inheritance, was found to strongly condition rock failure mechanisms and sizes of detaching blocks. Different estimates of design rock block volumes and masses were integrated into kinematic modelling, finally achieving a dynamic 3D reconstruction of the rock fall process. Based on modelling results, a remediation plan has been drafted focused on positioning and sizing of elastic barriers.

Keywords Rock fall · Structural analysis · Remote sensing · Cultural heritage · Appia route · Italy

Electronic supplementary material The online version of this article (https://doi.org/10.1007/s11069-020-03939-4) contains supplementary material, which is available to authorized users.

✉ E. Di Luzio
emiliano.diluzio@igag.cnr.it

Extended author information available on the last page of the article

1 Introduction

At the scale of rocky mountain ranges, inherited structural features can drive the onset and development of deep-seated gravitational slope deformations (DSGSDs) or large rock slope failures (e.g. Agliardi et al. 2001, 2009; Kellog 2001; Di Luzio et al. 2004; Ambrosi and Crosta 2006; Scarascia-Mugnozza et al. 2006; Esposito et al. 2007, 2014; Bianchi Fasani et al. 2011, 2014; Saintot et al. 2011; Penna et al. 2017). At the slope scale, the role played by local structural settings on discontinuity-controlled rock slope instabilities is also significant and can be difficult to unravel. In this case, the evaluation of the rock slope condition, aimed at hazard or susceptibility assessment, largely depends on a detailed structural/geomechanical analysis (Badger 2002; Coe and Harp 2007; Brideau et al. 2009; Massironi et al. 2011; Pedrazzini et al. 2011; Agliardi et al. 2013; Di Luzio et al. 2013; Humair et al. 2013; Stead and Wolter 2015; Guo and Wang 2018).

Among the types of slope instabilities, rock falls are defined as relatively small landslides that originate from the detachment of individual blocks—separated from a rock mass by structural/mechanical discontinuities—and evolve into subsequent downslope movement by flying, bouncing and rolling (Varnes 1978; Evans and Hungr 1993; Cruden and Varnes 1996; Hungr et al. 2014). Due to their unpredictability and high velocity, these events can cause casualties or great damage, even if the mobilized rock mass is small. Rock falls can affect communication routes, infrastructures, villages and cultural heritage elements (Tunusluoglu and Zorlu 2009; Wang et al. 2012; Di Luzio et al. 2013; Fanti et al. 2013; Margottini et al. 2015; Dinçer et al. 2016; Boldini et al. 2018).

This paper presents a study aimed at analysing the rock fall processes threatening the tract of the ancient Appia route which crosses the central Apennines at the Aurunci Mountain pass, between the modern towns of Fondi and Itri (Fig. 1). Nowadays, this stretch of the "Appia antica" is among the best preserved sections of the entire route (Quilici 1999, 2004, 2011), which was the first Roman consular road to be constructed between the 4th and 2nd cen. B.C.E. connecting the Tyrrhenian to the Adriatic coast of peninsular Italy and crossing the Apennine belt (Fig. 1, upper right insight). In the study area, at the Aurunci Mountain pass, the Appia route was built leaning against a steep rock slope composed of Jurassic and Cretaceous carbonates (Figs. 2a, b, 3). The slope is delimited by the narrow fluvial incision of the St. Andrea Valley and its morphogenesis has a clear tectonic inheritance (Di Luzio and Carfora 2018; Di Luzio 2019). Instabilities mainly concern the uppermost rock escarpments from which detaching blocks can reach the ancient road track, thus threatening elements of cultural heritage and safety of visitors.

The rock fall process was investigated by a multiple-step procedure, including the reconstruction of the local topography by an aero-photogrammetric survey and an inventory of the calcareous blocks found lying above the Appia pavement. The inventory was used as a constraint, in a back-analysis mode, for iterative modelling calibration. A kinematic modelling was then performed through a 3D simulation (e.g. Scioldo 1991, 2006; Agliardi and Crosta 2003; Dorren and Seijmonsbergen 2003; Crosta and Agliardi 2004; Guzzetti et al. 2002; Lan et al. 2007), based on a probabilistic approach (Li and Lan 2015 for a review) that allowed the prediction of trajectories, accumulation areas, run-out distances and kinematic parameters of dimensionless falling blocks (lumped mass approach). The modelling simulates single events of rock fall rather than a continuous accumulation of rock debris which are absent along the Appia route (Fig. 2a). The evaluation of possible trigger effects (rainfall, vegetation growth, seismic inputs) was not considered, being beyond the objectives of this work.

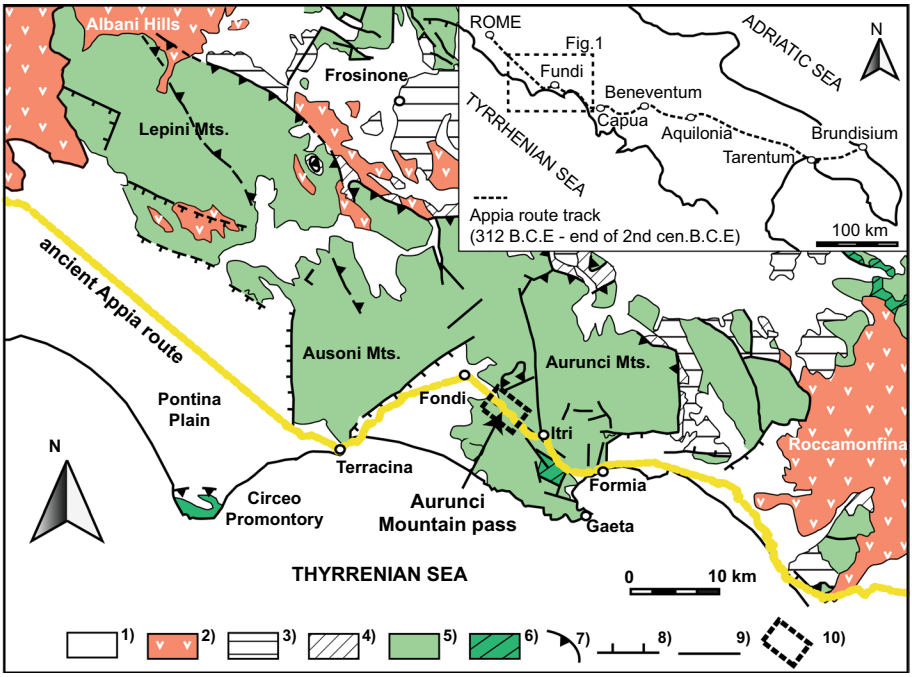

Fig. 1 Geological setting of the areas crossed by the ancient Appia route nearby the Tyrrhenian coastline (from Parotto and Tallini 2013, modified) and location of the study area. Legend: (1) Continental and marine deposits (Holocene-Upper Pleistocene), (2) Volcanic deposits (Upper-Middle Pleistocene), (3) Syn-orogenic siliciclastic deposits (Upper-Middle Miocene), (4) Liguridi Unit basinal deposits (Lower Miocene-Oligocene), (5) Carbonate platform deposits (Paleocene-Jurassic), (6) Carbonate platform deposits (Lower Jurassic-Upper Triassic), (7) Thrust, (8) Normal fault (dashed when inferred), (9) Strike-slip fault, (10) Location of the study area. Upper right inside: the track of the ancient Appia route across central-southern Italy

Field-based structural and kinematic analyses were completed to decipher deformation patterns and determine rock failure mechanisms and design blocks volumes. For inaccessible slope sectors, these operations largely benefit from the application of remote sensing methodologies, such as unmanned aerial system (UAS) and terrestrial laser scanner (TLS) surveys. Currently, integration among classic structural analysis and remote sensing methodologies has become a fundamental practice for rock slope characterization and risk assessment (Jaboyedoff et al. 2007, 2012; Sturzenegger and Stead 2009; Abellan et al. 2010, 2014; Sturzenegger et al. 2011; Gigli et al. 2012; Niethammer et al. 2012; Fanti et al. 2013; Riquelme et al. 2014; Martino and Mazzanti 2014; Baleani and Mazzanti 2017; Matasci et al. 2018; Fiorucci et al. 2018; Mazzanti et al. 2018).

The evidence of different failure mechanisms and magnitude of detachable blocks on the rock slope edge were related to variations in the style of tectonic deformation and the joint sets distribution in particular. Downstream of these results, multiple estimates of design block volumes were considered to upgrade the kinematic rock fall simulations into a dynamic model. A countermeasure plan was finally defined, consisting of placement and sizing of elastic barriers and directed towards the safeguard of local cultural heritage and tourist protection.

Fig. 2 **a** Geological map of the Aurunci Mountain pass and the St. Andrea Valley (modified from Di Luzio and Carfora 2018). Legend: (1) Alluvial deposits, (2) Terraced alluvial deposits, (3) Colluvial deposits, (4) Talus slope and paleo-landslide deposits, (5) Detritic and dolomitic limestone, dolomites (Upper Cretaceous, Turonian), (6) Detritic and dolomitic limestone (Upper Cretaceous, Cenomanian), (7) Micritic and detritic limestone and breccias (Lower Cretaceous, Aptian-Neocomian), (8) Detritic and oolitic limestone and dolomites (Neocomian-Upper Jurassic), **b** geological profile along trace *A*–*A*′–*A*″ (in the MF hanging wall block)

2 Geological setting and rock fall evidence

The Aurunci Mountains hosting the ancient Appia route belong to the peri-Tyrrhenian sector of the central Apennines (Fig. 1). At the Aurunci pass, the route track crosses mountain ridges composed of a carbonate sequence including limestone and dolomites. The youngest units (Neocomian-Upper Jurassic) crop out in the southern part of the study area, whereas the Lower and Upper Cretaceous units characterize the central and northern sectors. Quaternary continental units feature talus slopes, alluvial and colluvial deposits and are found within the St. Andrea Valley (Fig. 2a).

Southward, the morphotectonic setting is dominated by thrusting, folding and strike-slip faulting. A main ENE–WSW-oriented, recumbent anticline (Fig. 4a) is recognized in the hanging wall (HW ANT) of a south-verging thrust (Th1), along which the Lower Cretaceous sequence overlies the Upper Cretaceous section (Figs. 2b, 3). The thrust surface cut through a tight syncline which is paired with a wider, iso-oriented footwall anticline (FW ANT) developed in the Upper Cretaceous sequence and cut by a further thrust surface (Th2). Initial folding (T1) and subsequent thrusting (T2) features can be related to the middle Miocene orogenetic process in the westernmost part of the central Apennines (Cosentino et al. 2002; Centamore et al. 2007; Parotto and Tallini 2013).

These structures are clearly dissected by a NNW–SSE-oriented and counter-slope-dipping main fault (MF) showing strike-slip (left-lateral) kinematics (Fig. 4b, c). Transpressive features are developed corresponding to restraining bends, whereas bedding panel rotations are observed in the footwall block (Fig. 2a). The MF played a significant morphogenetic role since inaccessible or hardly accessible rock escarpments up to 20 m in height were generated in its hanging wall block (Fig. 4b); here, a damaged zone (hereafter DZ) presenting severe brittle deformation extends for approximately 10 m into the slope (Fig. 4c). The morphological expression of the MF decreases northwards, where rock escarpments are not higher than 6 m (Fig. 3). The age of the strike-slip event (T3) is unconstrained, but the relative chronology places it later than the Miocene events and prior to the Pliocene–Quaternary extensional tectonics (T4) that affected the Apennine belt (e.g. Cavinato and De Celles 1999; Galadini and Messina 2004; Patacca et al. 2008); this last phase produced NE–SW to NNE–SSW-oriented faults in the study area (Fig. 2a).

Rock falls from the slope edging the ancient Appia route are evidenced by several calcareous blocks found above the volcanic flagstone (Fig. 5a–d). Between 2013 and 2017, three rock fall failures were documented on different sections of the route track, whereas there is no record of other events in local chronicles or Italian landslide databases (Trigila 2007; Trigila and Iadanza 2008). Therefore, due to the lack of historical data, only a susceptibility analysis was pursued in this paper.

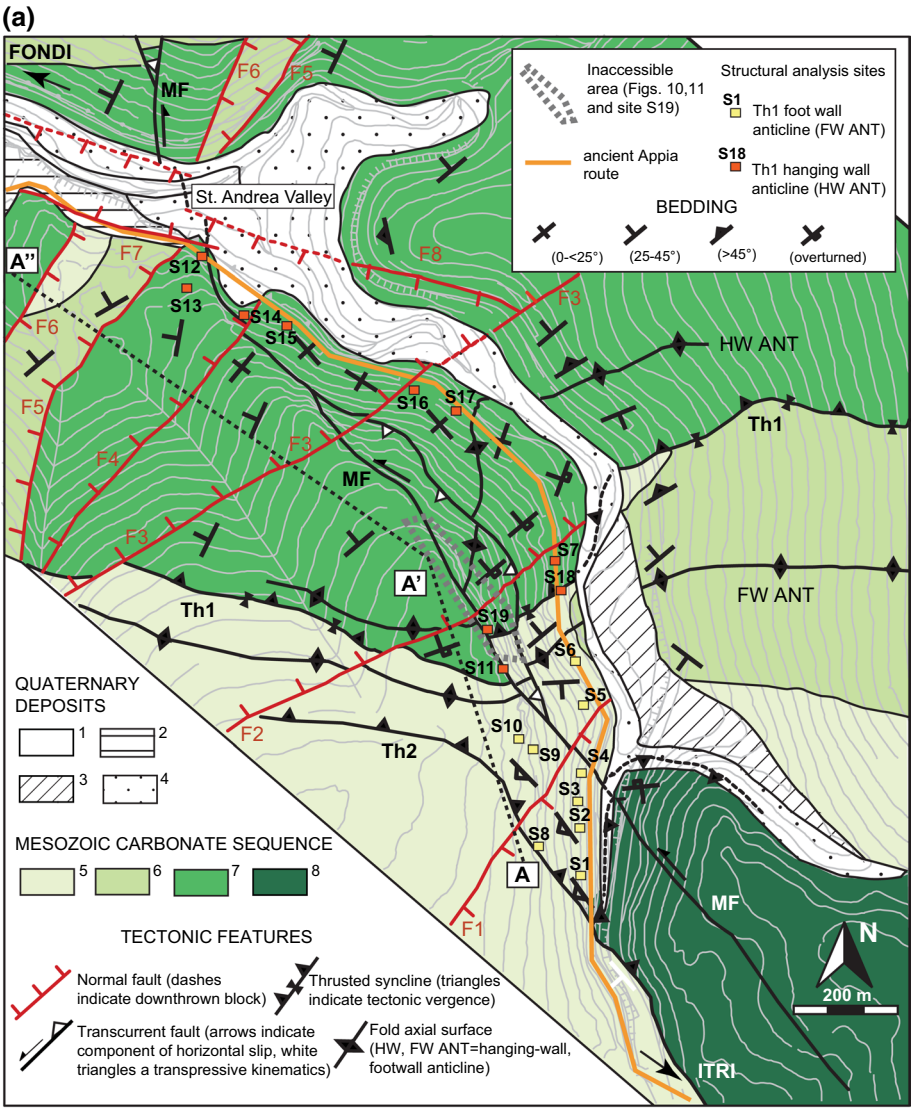
(a)
FONDI
MF
F6
F5
St. Andrea Valley
A''
F7
S12
S13
S14
S15
F8
F3
HW ANT
Th1
S16
S17
F6
F5
F4
F3
MF
A'
S7
S18
FW ANT
Th1
S19
S6
S11
S5
F2
Th2
S10
S9
S4
S3
S2
S8
S1
A
F1
MF
N
200 m
ITRI
Inaccessible area (Figs. 10,11 and site S19)
ancient Appia route
Structural analysis sites
S1 Th1 foot wall anticline (FW ANT)
S18 Th1 hanging wall anticline (HW ANT)
BEDDING
(0-<25°)
(25-45°)
(>45°)
(overturned)
QUATERNARY DEPOSITS
1
2
3
4
MESOZOIC CARBONATE SEQUENCE
5
6
7
8
TECTONIC FEATURES
Normal fault (dashes indicate downthrown block)
Thrusted syncline (triangles indicate tectonic vergence)
Transcurrent fault (arrows indicate component of horizontal slip, white triangles a transpressive kinematics)
Fold axial surface (HW, FW ANT=hanging-wall, footwall anticline)
(b)
A
SSE
Th2
Th1
FW ANT
HW ANT
A'
NNW
SE
A''
NW
F1
F2
F3
F4
F5
F6
thrusted syncline
Cretaceuos monocline
240m asl
200m
160m
120m
0m
200m
400m
600m

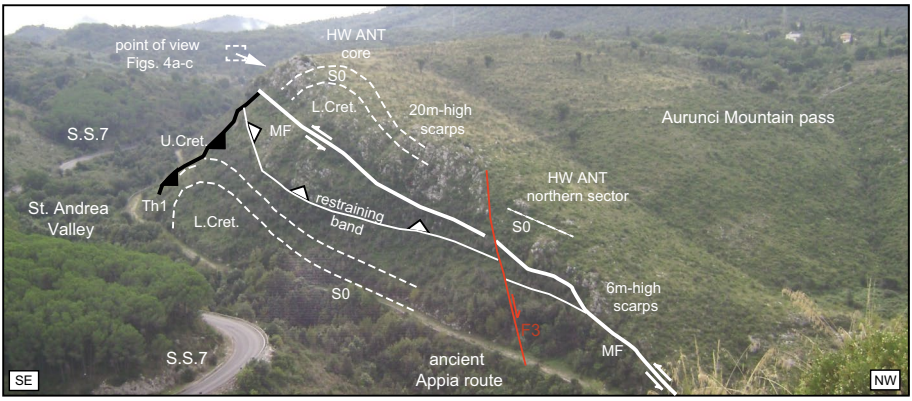

Fig. 3 Panoramic view of the St. Andrea Valley and the ancient Appia route at the Aurunci Mountain pass with line-drawing of main morphotectonic features of the analyzed rock slope. Legend: L. Cret., U. Cret, lower and upper cretaceous carbonates; HW ANT, hanging wall anticline; MF, main (strike-slip) fault; S0, bedding; Th1, thrust 1; S.S.7, modern Appia route

3 Methodologies

3.1 Aerial photogrammetry and remote sensing techniques

The topographic setting of the St. Andrea slope-to-valley system was reconstructed through an aerial photogrammetric modelling (1:3000 scale) described in Di Luzio and Carfora (2018). From aero-photogrammetry a DTM of the area was reconstructed (1 m cell size) and used to derive the shaded-relief map as shown in Fig. 6 (azimuth and altitude angle of the light source N315° and 45°, respectively).

Integrated surveys by multi-platform and multi-sensor remote sensing techniques were performed to obtain a widespread coverage of the rock slope and the inaccessible area in particular, with a resolution suitable for structural analysis. Photographic surveys through optical UAS flights and TLS measurements were planned, designed and completed considering the local slope characteristics (Fig. 7).

A network of targets was designed (Fig. 7a) including fifteen rectangular and painted PVC plates (21 × 30 × 0.4 cm) equipped with a reflecting target in central points (Fig. 7a′) and used for both UAS and TLS surveys (St1–15). Based on a multi-platform configuration (i.e. different points of view for the same slope sector), these hybrid targets were also equipped with a pointing system based on a 3D oscillating steel head (Fig. 7a″), allowing their proper orientation. The target network was completed with the installation of seven round reflecting targets (T1–7), having diameters ranging from 5 to 10 cm, for the TLS surveys only (Fig. 9a‴). The accurate (centimetre accuracy) 3D geographic coordinates of the targets network (in the WGS84 datum) were collected using a GNSS system in Real-Time Kinematic (RTK) mode, with the support of the Italian GNSS permanent network for differential corrections.

Optical UAS surveys were performed by a multi-copter drone equipped with a GO-PRO HERO 3 camera. Nine flights were completed, allowing the collection of more than 4800 photographs. Both nadir and oblique images (for the steepest slope sectors) were collected.

For the TLS survey, a Riegl VZ1000 system was used (instrumental range up to 1400 m), equipped with a high-resolution calibrated digital camera for the acquisition of

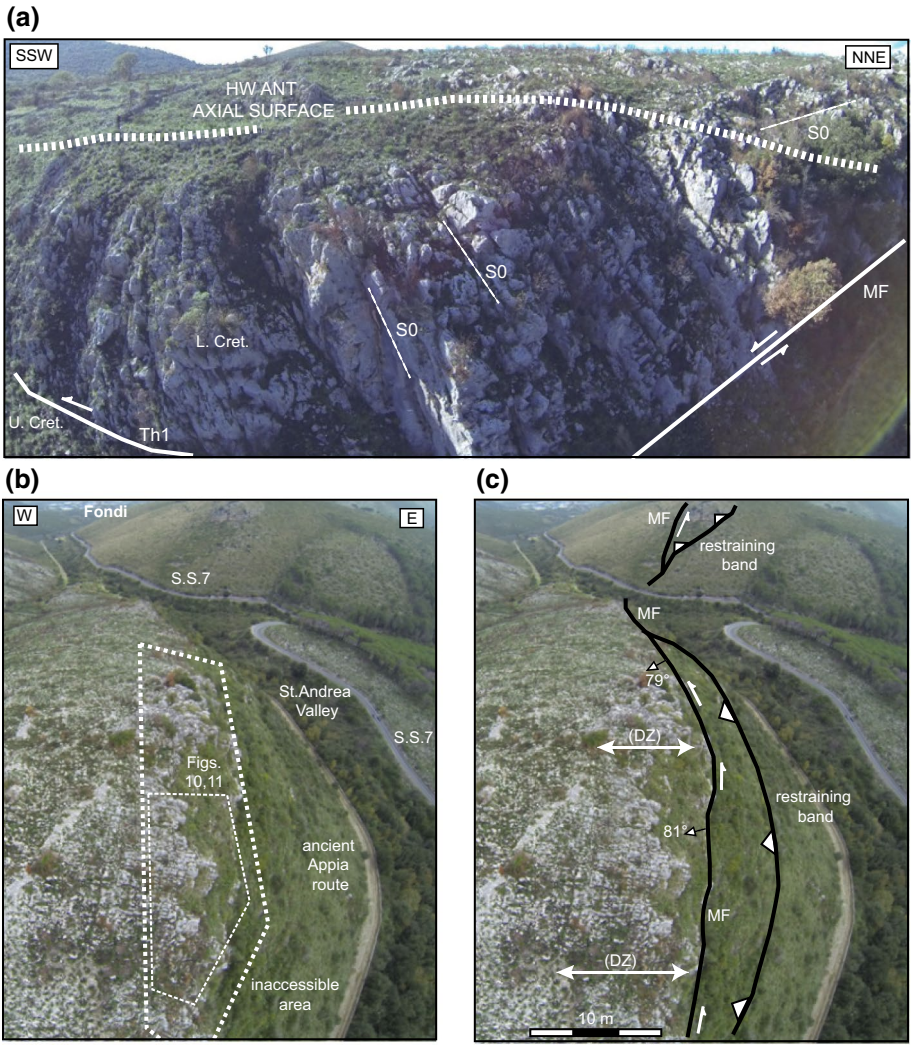

Fig. 4 Unmanned Aerial System (UAS) images of: **a** the southern slope sector with the recumbent HW ANT and the reverse bedding (S0) in the Lower Cretaceous (L. Cret.) sequence, **b** the rock slope longitudinal profile, **c** the MF trace and the extension of the damaged zone (DZ) in its hanging wall block

real-colour 3D models. Six different scan positions were set (TLS1–6 in Fig. 7) to reduce the shadow zones. Data collected from each scan position were processed and aligned to draw a single high-density point cloud containing more than 700 million points. Finally, each point of the 3D model was assigned an RGB value based on the optical images collected by the digital camera (Fig. 7b), thus allowing the generation of a 3D real-colour point cloud imaging the entire (virtual) slope.

Data acquired through the TLS survey were processed by Discontinuity Set Extractor (DSE), an open-source software package dedicated to detection of structural discontinuities from 3D point clouds. By adopting a semi-automatic approach, the error related to the

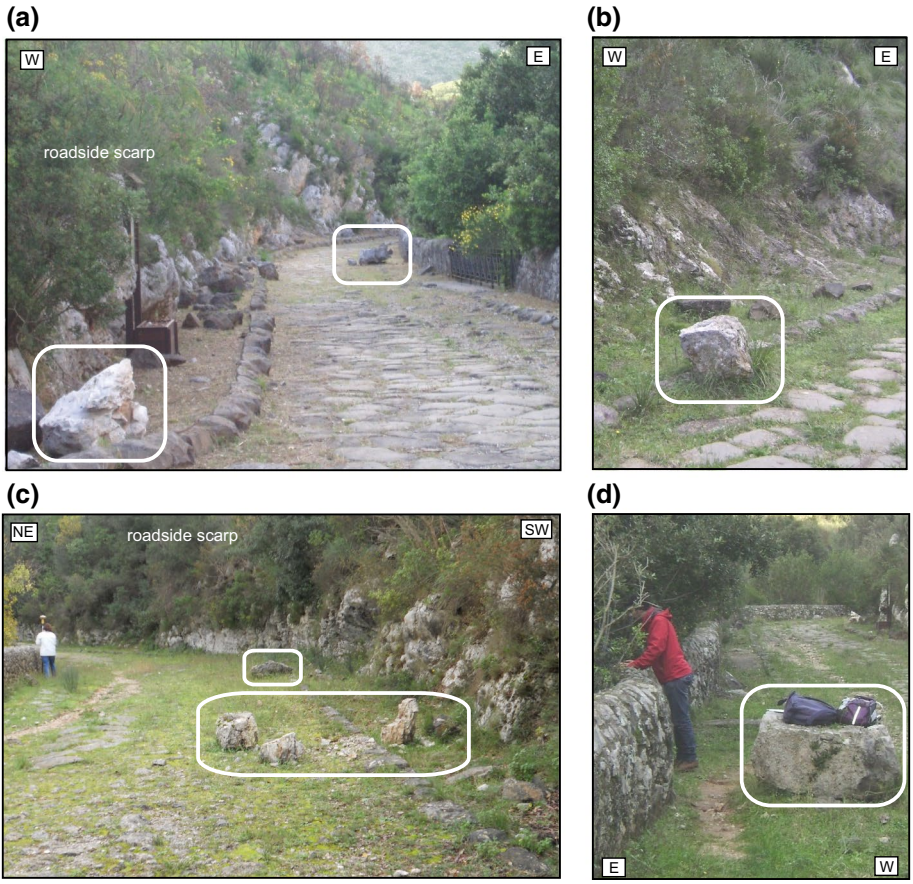

Fig. 5 Evidence of calcareous rock blocks (in white rectangles) fallen on the volcanic flagstone of the ancient Appia route, featuring different volumes and shapes: **a** wedge-shaped, **b** sub-cubic, **c** sub-cubic and prismatic, **d** parallelepiped-shaped

operator subjectivity was reduced; the main joint sets were detected and classified based on the geometric distribution of points in the space. Following Riquelme et al. (2014), this methodology was developed through the following steps: (1) local curvature calculation, which consists of the nearest neighbour searching and determination of the discontinuity (plane) orientation in every point; and (2) statistical and cluster analysis of planes to infer main orientations (dip/dip direction) representing the different discontinuity sets (user-controlled operation).

3.2 Field-based structural analysis, failure mechanisms and block volumes assessment

Structural analysis was performed at 18 sites on the slope (Figs. 2a, 8a), outside an inaccessible or hardly accessible area (see Figs. 4b, 6, 7a, b). Dip direction/dip data were collected together with measurements and observations regarding fracture spacing, length, aperture;

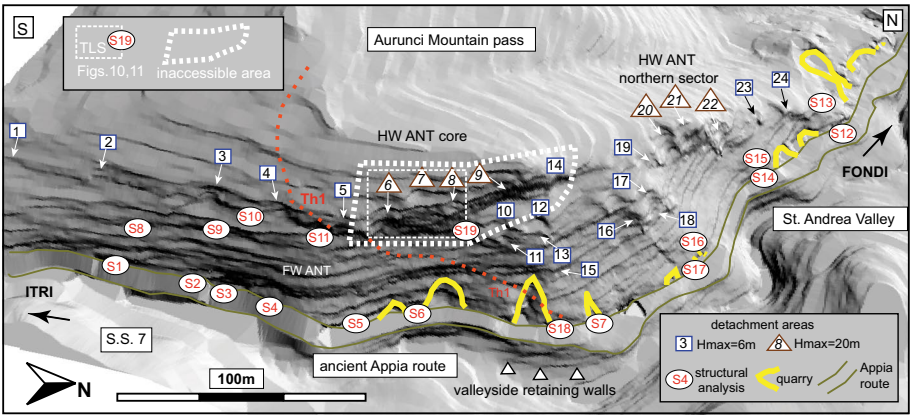

Fig. 6 3D shaded relief map of the study area with indication of 24 detachment areas identified as sources of past rock fall events. Sites of field-based (S1–S18) and TLS-aided (S19) structural analyses and location of rock quarries along the Appia route (Di Luzio and Carfora 2018) are also reported

etc., according to ISRM 2007 (Online Resource 1). Lower hemisphere, equal-angle projections were drawn for all sites to delineate joint sets within the structural domains as presented in Fig. 8a: (1) the hanging wall anticline (HW ANT) of the south-verging thrust Th1; the footwall anticline (FW ANT); and (3) the strike-slip damaged zone (DZ), which is superimposed on the others.

Compatibility of rock mass discontinuities to different failure mechanisms was assessed through the Markland analysis (1972). For this purpose, a basic friction angle $\Phi_b = 38°$ for a generic unweathered joint surface in dolomitic limestone was assumed by literature (Hoek and Bray 1981; Cruden and Hu 1988; Bruce et al. 1989; Goodman 1989; Gonzalez de Vallejo et al. 2005; Waltham 2009). The values of the residual friction angles Φ_r were then estimated according to the Barton and Choubey (1977) equation $\Phi_r = (\Phi_b - 20°) + 20(r/R)$, where r and R are the Schmidt's hammer rebound number on weathered and unweathered fracture surfaces, respectively. Sclerometric measures were taken at sites S1–S8 and S16–S17 (Fig. 8a). After calculations, an average value of $\Phi_r = 31°$ was used in the planar sliding, wedge sliding and toppling failure analyses.

Finally, the results of structural and Markland analyses at sites S1–S18 and in the inaccessible area (site S19)—with the aid of the TLS survey—were used to reconstruct the geometries and volumes of potentially unstable rock blocks by means of the ROCSCIENCE software suite.

3.3 Rock block inventory and modelling assumptions

A geo-referenced rock block inventory including 80 elements was completed. Calcareous blocks are present throughout the entire route of the Via Appia, even if with an uneven distribution (Fig. 8b). Downslope propagations of detached rock blocks were simulated through the ROTOMAP® software code (Scioldo 1991, 2006) that implements a probabilistic model by calculating a large number of 3D trajectories and adopting a lumped mass approach, i.e. only the boulder centre of mass is tracked (kinematic modelling). Therefore, the effects on trajectories of block size and shape are neglected (Ritchie 1963; Evans and Hungr 1993; Guzzetti et al. 2002; Agliardi and Crosta 2003; Dorren 2003; Lan et al. 2007).

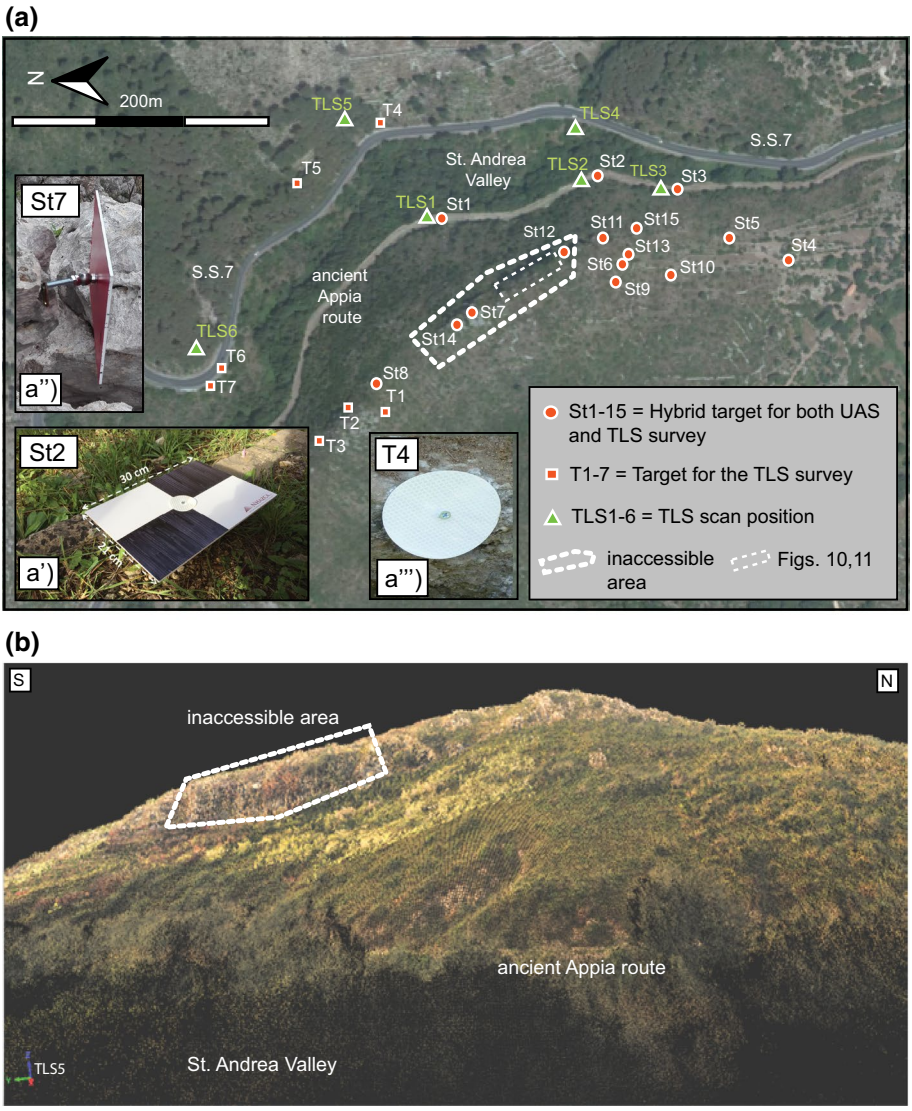

Fig. 7 **a** The target network for remote sensing, **a′** PVC target for UAS and TLS surveys (St1–15), **a″** detail of the pointing system, **a‴** reflecting target for the only TLS surveys (T1–7), **b** 3D real colour point-cloud of the investigated slope from TLS data elaboration (virtual slope)

Successively, the implementation of the kinematic simulations in a dynamic modelling is achieved considering a design block with a reference volume and mass.

For the assessment of model inputs the following assumptions were made: (1) starting points were set at the bases of former detachment areas (Figs. 6, 8b); (2) two initial starting velocities $[V_0 = Cd\sqrt{(2gH)}]$ were distinguished considering detachments from two groups of rock escarpments with different maximum heights ($H = 6$ or 20 m in Fig. 8b, from DTM analysis); (3) possible impacts along non-vertical scarps were

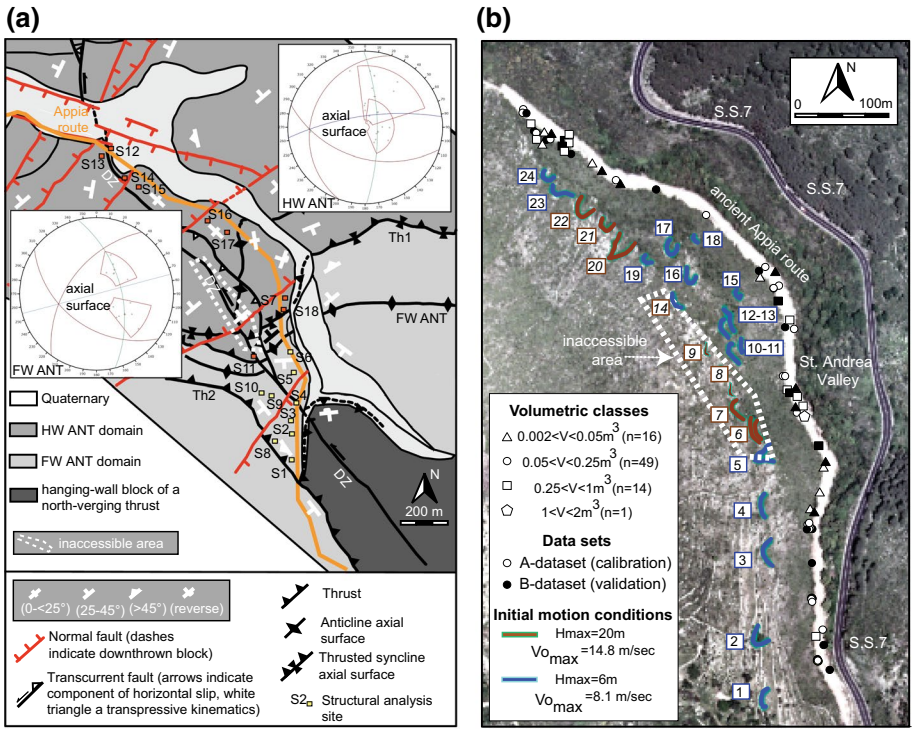

Fig. 8 **a** Structural sketch of the study area showing geological domains, sites of field-based structural analysis and reconstruction of the FW ANT and HW ANT axial surfaces, **b** base map with the rock block inventory (volumetric classes and A-, B-datasets) and position of detachment areas with different maximum height (H_{max}) and starting velocities V_{0max}

considered by imposing the coefficient of damping Cd = 0.75 and then slightly reducing V_0 along starting lines. Terrain classes were identified by interpretation of UAS-derived images and field checks. Then, following a literature review, initial values of the elastic restitution coefficients (Kn and Kt) and dynamic friction angle (Φ_d) were assigned to each terrain class to account for the loss of energy during bouncing and rolling phases of motion (Table 1).

Modelling calibration (through a back-analysis procedure) was focussed on setting different ranges of values for Kn, Kt and Φ_d parameters. Basically, the model was calibrated considering the blocks found on the Appia road and few others observed right above the roadside scarp. The thick arboreal vegetation prevented from distinguishing any blocks that stopped on the intermediate part of the slope. The few blocks visible downslope, at the bottom of the St. Andrea Valley, were ignored since they could have been transported or moved from their original position by flood events. The simulation process was repeated until modelling results matched the A-dataset (48 blocks corresponding to 60% of the entire rock block inventory); the B-dataset, including 40% of the observed blocks (32 features), was instead kept aside during modelling and used later for validation (Fig. 8b).

Table 1 Literature review of Kn, Kt and Φ_d values for terrain classes distinguished on the slope

	Calcareous bedrock (CB)			Arboreal vegetation (AV)		
	Kn	Kt	Φ_d	Kn	Kt	Φ_d
Broili (1973)	0.75–0.80 (K)					
Piteau and Clayton (1987)	0.65–0.75	0.8–0.9				
Pfeiffer and Bowen (1989)				0.30–0.33	0.8–0.83	
Giani (1992)				0.25		
Budetta and Santo (1994)	0.20	0.53				
Azzoni and de Freitas (1995)	0.51–0.92 (K)					
Azzoni et al. (1995)	0.75–0.90 (K)	0.40–0.45				
Chau et al. (2002)	0.40–0.60	0.65–0.90				
Agliardi and Crosta (2003)				0.35	0.65	0.55
Guzzetti et al. (2003)	0.65	0.80	0.30			
Guzzetti et al. (2004)	0.65	0.75	0.25			
Ferrari et al. (2013)	0.60	0.80	0.20	0.20	0.40	0.70
Average min/max values	0.573–0.674	0.744–0.811	0.287–0.30	0.275–0.282	0.616–0.626	0.625
Average (before calibration)	**0.623**	**0.777**	**0.293**	**0.278**	**0.621**	**0.625**
Average (after calibration)	*0.60*	*0.70*	*0.35*	*0.20*	*0.4*	*0.75*
Variation (%)	−4.76%	−9.10%	+16.28%	−14.38%	−35.58%	+16.67%
	Shrub-like vegetation (SV)			Flagstone (FL)		
	Kn	Kt	Φ_d	Kn	Kt	Φ_d
Pfeiffer and Bowen (1989)	0.30–0.33	0.83–0.87		0.37–0.42	0.87–0.92	
Pfeiffer and Higgins (1990)		0.82–0.85		0.37–0.42	0.87–0.92	
Azzoni et al. (1995)				0.75(K)	0.40–0.45	
Agliardi and Crosta (2003)	0.33	0.75	0.50	0.45	0.7	0.6
Ferrari et al. (2013)				0.4	0.9	0.2
Average min/max values	0.315–0.33	0.80–0.823	0.50	0.468–0.488	0.818–0.838	0.400–0.417
Aver. (before calibration)	**0.315**	**0.812**	**0.50**	**0.478**	**0.828**	**0.408**
Average (after calibration)	*0.38*	*0.60*	*0.60*	*0.40*	*0.68*	*0.50*
Variation (%)	+17.10%	−26.10%	+16.67%	−16.32%	−17.87%	+18.4%

K, undifferentiated values

Averaged values before calibration and final values after calibration (with percentage variations) are reported in bold and italics, respectively

4 Results

4.1 Aerial photogrammetry

The topography setting of the St. Andrea slope-to-valley system, which was reconstructed through a DEM surface derived from aerial photogrammetry, is characterized by 24 half-circle or wedge-shaped rock scars in the uppermost and middle portions of the carbonate ridge. After field checks, these scars were assumed to be source areas (detachment zones) of past rock fall events. Figure 6 shows how the identified areas cover almost the entire length of the upper escarpment. Instead, rock cuts in the lowermost part of the slope, nearby the Appia route, were recognized as rock quarries by Di Luzio and Carfora (2018).

4.2 Structural analysis from field surveys and TLS-UAS data elaboration

The results of field-based structural analysis are reported in Fig. 9 and Table 2. Recurring and secondary joint sets can be distinguished, as well as differences in deformation patterns among structural domains. The joint sets J1, including NNE–SSW- to NE–SW-oriented fractures, is present throughout the whole area, both in the FW ANT (sites S1–6; S8–10 in Fig. 8a) and the HW ANT (sites S11, S13, S14, S16, and S17) domains. The joint system J2, featuring NW–SE-oriented and NE-dipping, low- to medium-angle (20°–45°) discontinuities, characterizes the FW ANT, while it is absent in the HW ANT (apart sites S7, S11 and S18). A third recurring joint system, J6, is observed within the DZ or near the MF trace, at sites S4, S14–16. Secondary joint sets (J3, J4, J5 and J7) are distributed both in the FW ANT and HW ANT domains. Among all joint sets, J1 shows significant lengths and wider openings (Online Resource 1); locally, J1 fractures can be characterized as mega-joints cutting through the whole rock slope. Bedding (S0) is also reported as a mechanical discontinuity for all sites in Fig. 9. Within the DZ, data measured in the MF footwall or hanging wall are distinguished, and an anti-clockwise bedding rotation is evidenced in the first case (sites S12, S14–17).

Table 2 compares the results from field-based structural analysis with those obtained from TLS data elaboration on the entire length of the inaccessible area (Fig. 4b). Figure 10 focuses on the southern sector of the same area, which is identified as site S19, and illustrates the results of the DSE analysis. TLS points located on joints with different orientations are plotted on the cloud by different colours and the spatial distribution of eight main joint sets (JA–JH) is reconstructed. Approximately 26% of the points fall on gently-dipping discrete surfaces belonging to JA, which can be identified with J2. The second prevailing joint system is JB (14,6%), which is recognized as J6. The J1 joint set is also present (JD, 9.4%), and the other sets evidenced by field-based structural analysis can be found.

High-resolution images obtained from the UAS survey allowed overall views of the area and helped outline the structural setting. For instance the front view in Fig. 11a, showing part of the slope sector imaged in Fig. 10, evidences how the discontinuities belonging to set J1 can isolate rock pillars as high as the entire escarpment (20 m) and between 7 and 8 m wide. Considering the entire thickness of the DZ associated with the MF (10 m) to infer the depth of the blocks, their volume would range between 700 and 800 m^3. However, the UAS nadir image reported in Fig. 11b, c clearly shows that rock pillars are fragmented in smaller blocks due to significant rock mass disruption into the DZ.

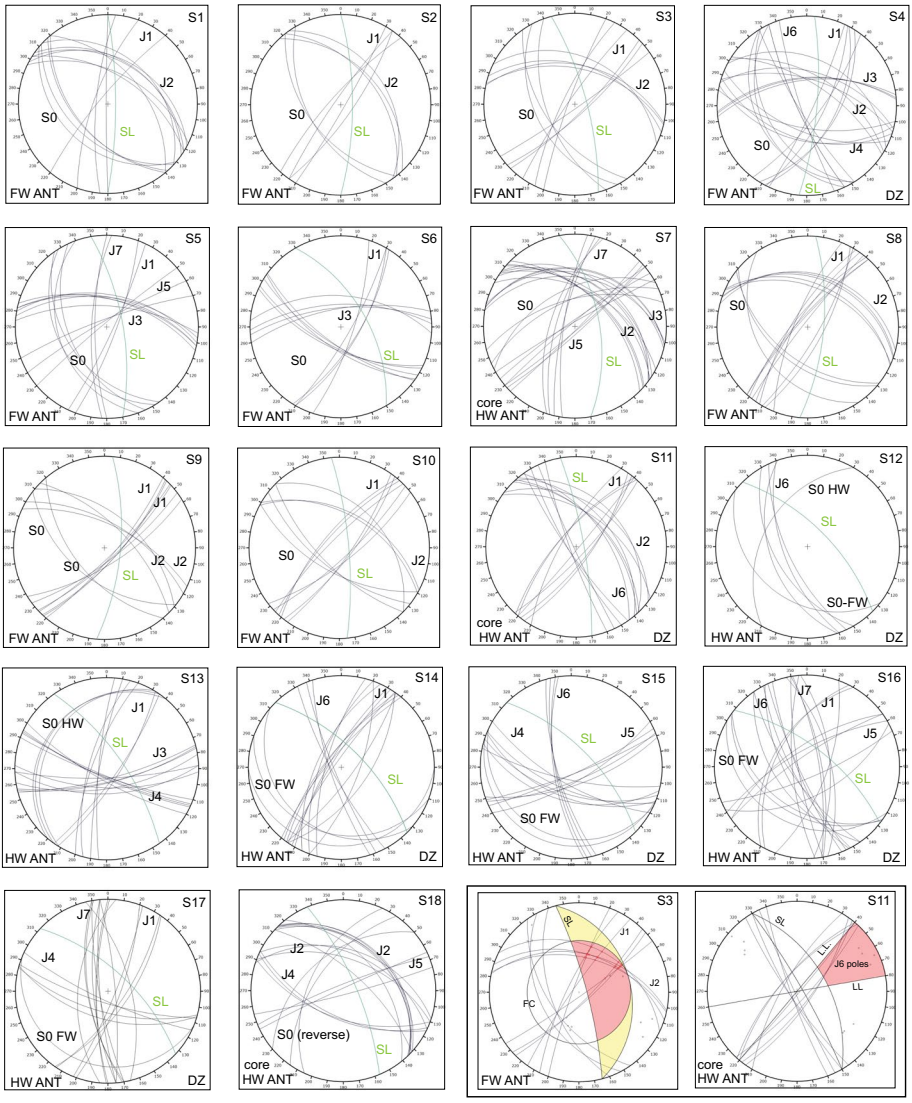

Fig. 9 Lower hemisphere, equal angle projections for sites of structural analyses S1–S18. Legend: Ji, joint set; SL, slope orientation; S0 FW and S0 HW, bedding within the MF foot wall and hanging wall block, respectively; for other terms see previous figures. Lower right box: Markland analysis for wedge sliding and toppling failure mechanisms at sites S3, S11, respectively. Legend: FC, friction cone; LL, lateral limits

4.3 Kinematic analysis

Table 3 shows the results of the Markland analyses performed at sites S1–19. In the FW ANT domain, wedge sliding failure mechanisms are favoured by the geometric combination between the J1 and J2 joint sets (see Fig. 9, lower right box, site S3). Compatibility with wedge sliding is also assured by further joint combinations (J1, J3 and J5) or intersections between joint surfaces belonging to a single joint system. Toppling is also possible

Table 2 Joint sets observed at sites S1–18 ad S19 and hypothesis of correspondence between field-based and TLS-aided structural analyses

Field-based structural analysis (sites S1–18)								
Set	J1	J2	J3	J4	J5	J6	J7	
Dip Direction (main plane)	N326/N142	N38	N170/N350	N201	N343/N163	N245	N272/N88	
Dip	71/67	42	73/78	69	78/71	79	74/79	
Semi-automatic 3D point clouds elaboration (site S19)								
Set	JA	JB	JC	JD	JE	JF	JG	JH
Dip direction (Main plane)	N55	N235	N101	N307	N176	N298	N198	N277
Dip	41	76	83	85	81	39	41	86
Percentage (%)[a]	26.3%	14.6%	9.8%	9.4%	6.3%	3%	2.5%	2.5%
Correspondence	J2	J6	J7	J1(~S0)	J3	(?)	J4	J7

Main planes were calculated separately for opposite dip directions in the same joint set

[a]Point percentage from point clouds

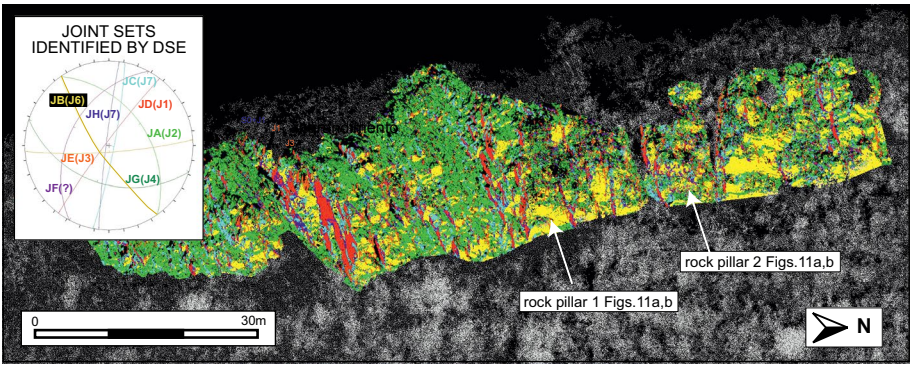

Fig. 10 Front view of the virtual slope (from TLS data) after DSE analysis. A different colour was assigned to each joint set and used for cyclographs in the stereonet

and may develop on S0 and W-dipping fractures belonging to the J1 (site S8) and J6–J7 sets (sites S4 and S5, respectively). Planar sliding is expected only at sites S4 and S8, where it may occur along east-dipping J1 discontinuities.

Due to the absence of J2 (Fig. 9), wedge failures are partially inhibited in the northern sector of the HW ANT (sites S12–17); such kind of failure can occur only at a few sites (S13, S16, and S17) due to the combination of other joint sets. In contrast J2 is documented within the core of the same HW ANT (sites S7, S11, S18) and indicated as the prevalent discontinuity system by DSE analysis (S19, Fig. 10; Table 2). Toppling in the HW ANT and within the DZ domain can be driven by failures along S0, J6 (Fig. 9, lower right box, S11) and, subordinately, J4. Joints and slope geometric attitudes are again unfavourable to planar sliding (apart at site S18 along J2 fractures).

Finally, Table 3 reports volume estimates for potential detachments at sites S1–18 and S19 for different failure mechanisms. Minimum and maximum values reflect corresponding variations in joint spacing.

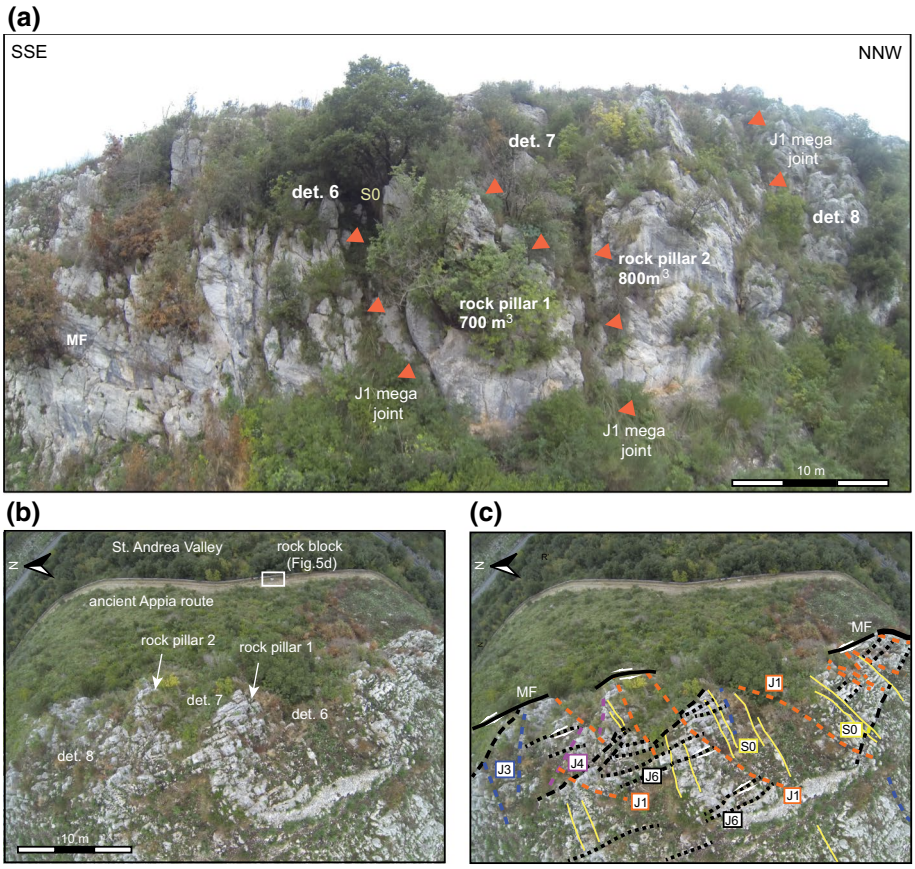

Fig. 11 **a** UAS image of the area investigated by TLS in Fig. 10, showing the J1 mega-joints, two rock pillars and some detachment areas (dt. 6–8); **b** top view of the same area; **c** line-drawing of joints sets and S0 into the DZ

5 Rock fall modelling

The statistical sample of rock blocks detected on the ancient Appia route shows a bimodal volumetric distribution over a range spanning from 2×10^{-3} to 1.75 m^3 (Fig. 12a), with a mean value of 0.343 m^3. Before arresting, rock blocks propagate down a slope mainly covered by arboreal and shrub-like vegetation (AV and SV in Fig. 12b), with narrow outcrops of the calcareous bedrock (CB).

Graphical outputs of the kinematic modelling are presented in Fig. 13. The rock fall simulations were eventually accepted when 75% of inventoried rock blocks (A-dataset in Fig. 8b) were found to be located within a 2 m-wide buffer zone around accumulation areas (Fig. 13a). Buffering was imposed to account for the uncertainty in GPS localizations of rock blocks and their possible remobilizations from the original arrest points on the road track. Model validation was performed by comparing results with the B-dataset (Fig. 8b); adopting the same buffering rule, more than 70% of blocks resulted to be inside accumulation areas identified by modelling.

Table 3 Failure mechanisms for different joint combinations as identified by the Markland analysis at sites S1–19 and within different structural domain (FW ANT, HW ANT, HW ANT core and DZ)

Sites	Failure mechanisms and rock block volumes (min. and max. in m^3)					
	Planar sliding	Vol.	Wedge sliding	Vol.	Toppling	Vol.
FW ANT						
S1			(J1 + **J2**); (***J2***)	0.4–1.2	J1 (NW–dipping)	1.5–2.5
S2			(J1 + **J2**)	0.1–0.5	S0	0.8–1.6
S3			(J1 + **J2**); (*J1*); (***J2***)	0.2–0.7	S0	1.2–2.3
S4 (DZ)	J1 (SE-dipping)	0.9–2.1	(J1 + **J2**) (J1 + J3); (**J2** + J3); (***J2***); (*J4*)	0.6–1.7	J6	1.9.–3.0
S5			(J1 + J3); (J1 + J5); (J3 + J5); (*J1*)	0.1–0.3	J7, S0	1.5–2.4
S6			(J1 + **J3**); (*J1*)	1.3–2.6		
S8	J1 (SE-dipping)	0.5–0.6	(J1 + **J2**); (*J1*)	0.8–1.8	J1 (NW-dipping)	1.4–2.7
S9			(J1 + **J2**); (*J1*); (***J2***)	2.2–3.3		
S10			(J1 + **J2**); (***J2***)	0.6–0.9		
		Min/max		Min/max		Min/max
		0.5–2.1		0.1–**{3.3}**		0.8–3.0
HW ANT northern sector						
S12 (DZ)					J6; S0 FW	1.3–2.0
S13			(*J1*); (*J3*)	0.5–1.4	J4	
S14 (DZ)					J6	2.0–2.5
S15 (DZ)					J4, J6	0.8–1.9
S16 (DZ)			(J1 + J5); (J1 + J7)	0.6–1.3	J6	1.8–2.5
S17			(J1 + J7)	1.2–1.7	J4	0.8–1.8
		–		Min/max		Min/max
		–		0.5–1.7		0.8–**{2.5}**
HW ANT core						
S7			(**J2** + S0); (J5 + S0); (*J5*)	0.3–1.2	J1 (NW-dipping)	1.7–2.6

Table 3 (continued)

Sites	Failure mechanisms and rock block volumes (min. and max. in m^3)					
	Planar sliding	Vol.	Wedge sliding	Vol.	Toppling	Vol.
S11 (DZ)	J1 (SE-dipping)	0.4–1.1	J1 + **J2**	1.4–3.2	J6	2.5–5.8
S18	J2		(S0 + **J2**); (**J2** + **J5**)	0.2–0.9		2.5–4.3
S19 (TLS)			(JA + JD alias **J2** + J1)	4.3 (aver.4)	JB, JD (alias J6, J1 NW-dipping)	**{6.7}** (aver.6)
			JA + JE (alias **J2** + J3)			
		Min/max		Min/max		Min/max
		0.4–1.1		0.2–3.2		1.7–**{6.7}**

J2 is reported in bold whereas single joint sets giving wedge failures are in italics. Block volumes calculated for each mechanism are indicated, as well as values chosen for estimates of design blocks (in braces and bold)

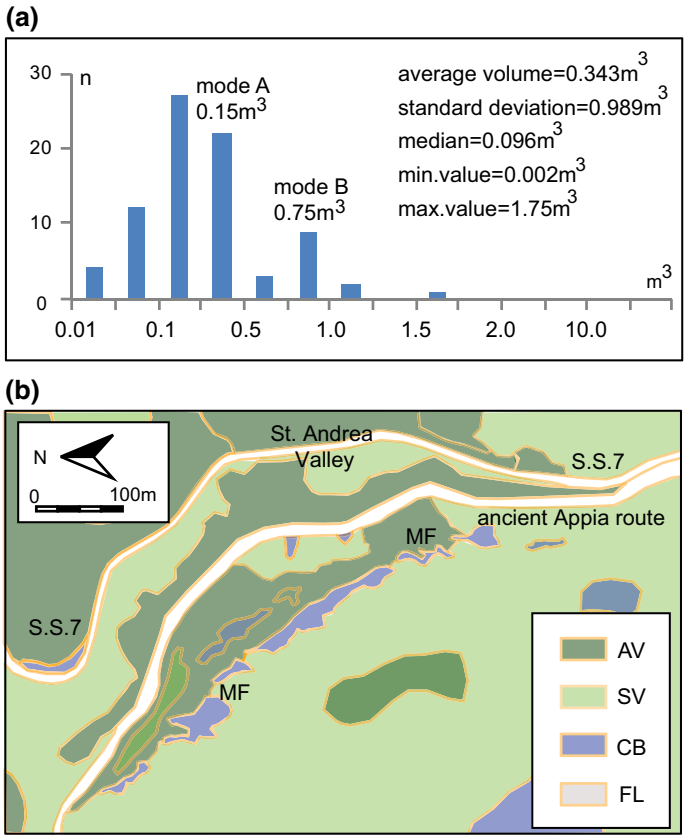

Fig. 12 **a** Statistical analysis of rock block volumes, **b** terrain classes (slope zonation). Legend: AV, arboreal-like vegetation; CB, calcareous bedrock; FL, flagstone; SV, shrub-like vegetation

Table 1 reports both the initial (averaged from literature) and final (after calibration) values of Kn, Kt and Φ_d. Differences among values are $<20\%$ except for AV and SV terrain classes which show a decrease in Kt values after calibration equal to 35.6% and 26.1%, respectively.

A number of 3D trajectories equal to the products between starting points, initial velocities and falling directions were simulated (160 and 392 from 20 to 6 m high scarps, respectively). Basically, motions take place by rolling and show minimal diversions from the maximum slope direction (Fig. 13b). Rock blocks can reach the Appia route at different sections; the main concentrations are foreseen beneath source areas 6–8, 12–15 and 20–24 (Fig. 13a). A contour map of the specific kinetic energy ($E_{cin} = 1/2v^2$) gained by dimensionless blocks along their paths is presented in Fig. 13c. Maximum values of 200–250 m^2/s^2 are reached in the central and north-western sectors by blocks detached from the highest escarpments (20 m). E_{cin} values for escarpments with a lower height (6 m) do not exceed 150 m^2/s^2. The last model output illustrates the distribution map of the bouncing heights (Fig. 13d). Rebounds higher than 2 m can occur only for rock falls from 20 m-high escarpments. In these cases, blocks can reach the roadside scarp (Fig. 5a, c) with rebound heights ranging from 2 to 6 m. Higher

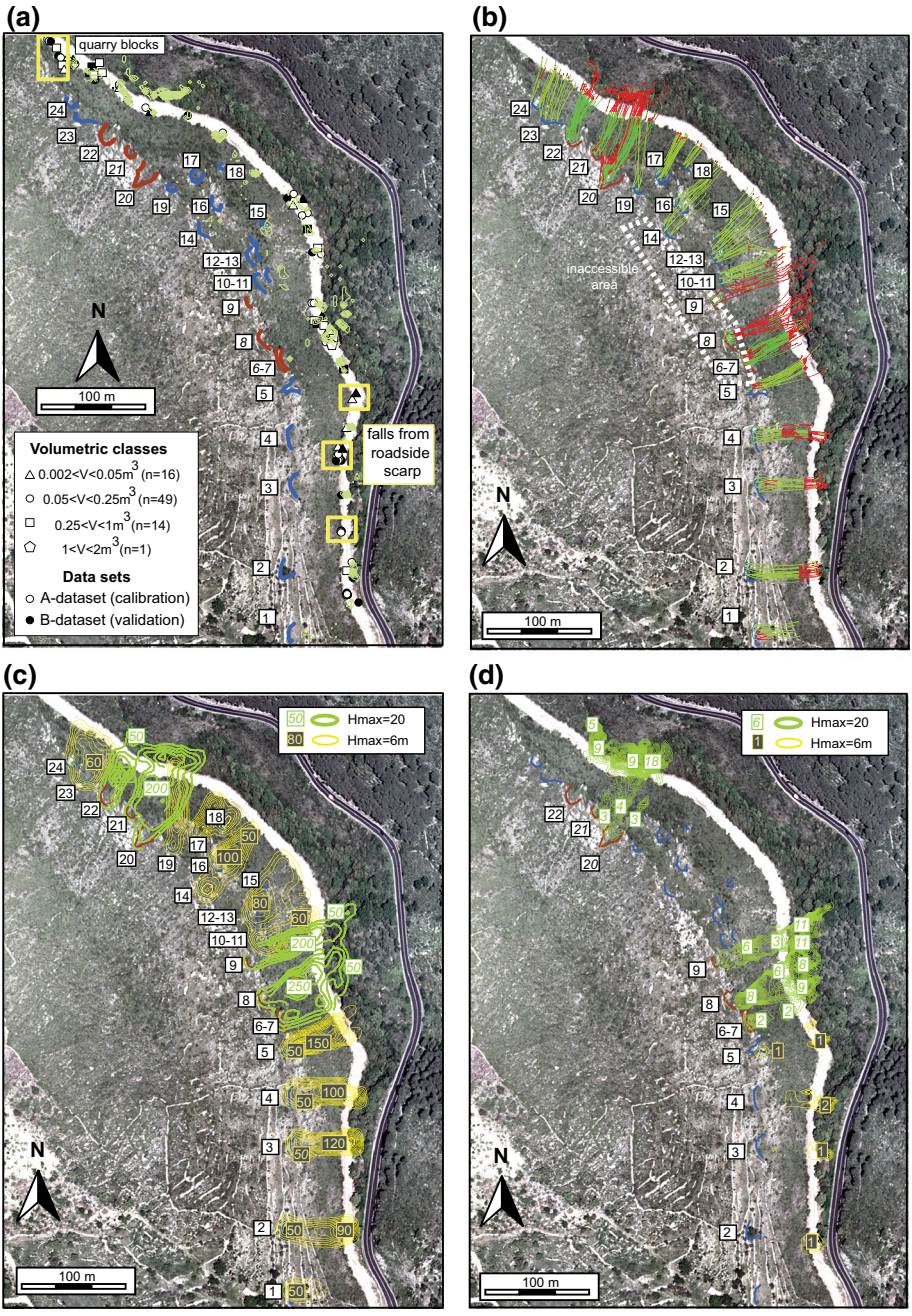

Fig. 13 **a** Contour map of arrest points (ppm/m^2) superimposed on the rock block inventory (contour interval 250 × 10^6/m^2, **b** simulated trajectories: pale (green) lines indicate rolling and sliding along slope, dark (red) lines bouncing; **c** map distribution of the specific kinetic energy (m^2/s^2). Contour interval is 50 and 10 m^2/s^2 for thick and thin (green and yellow) lines, respectively; **d** map distribution of bouncing heights (m) with a unique contour interval (0.5 m)

values (8–18 m) are referred to as blocks flying over the Appia retaining walls into the St. Andrea Valley.

6 Discussion

Localization of former source areas is of primary importance for rock fall modelling (Aksoy and Ercanoglu 2006; Copons and Vilaplana 2008; Vangeon et al. 2001; Guzzetti et al. 2003; Wieczorek et al. 2008). Despite the lack of historical records, 24 detachment areas were identified on the investigated slope (Figs. 6, 8b). From these areas rock fall simulations were run, with interactions between rock blocks and the slope being controlled by coefficients of normal and tangential restitution and the friction angle.

The last model simulation obtained after model calibration (Fig. 13) implies minor variations in initial dynamic parameters (Table 1). The only significant differences regard the reduced Kt values for the AV and SV slope classes after calibration; this result may be explained by admitting a significant role for vegetation in decreasing elastic energy during rebounds. Validation of modelling results by comparison with the B-dataset in the rock block inventory was satisfactory. Few rock block clusters north of detachment area 24 and in the southern sector, below detachment areas 1–4, seem inconsistent with the model results (Fig. 13a). In the first case, the presence of many rock blocks is imputed to the excavation of rock quarries (see Fig. 6) for the supply of stone materials during the road construction (Di Luzio and Carfora 2018), whereas falls from the roadside scarp (Figs. 5a–c) can be invoked to explain the other situation.

Upgrading from kinematic modelling of falling dimensionless blocks to a dynamic modelling for the design of countermeasures required the choice of a "design block" with a specific volume and mass (e.g. Pantelidis and Kokkalis 2011; Bourrier et al. 2015). This can be defined as the most likely or the largest block detaching from the rock slope. Shape and dimension of the design block depend on joint characteristics and the failure mechanism prevailing within the rock mass, which on the slope overhanging the Appia route are both differentiated depending on deformation patterns originating during the T1–T4 tectonic events (Fig. 14).

In the FW ANT domain and into the core of the HW ANT two main joint sets prevail, i.e. J1 and J2 (Fig. 9). The first set is persistent throughout the area and is considered to be part of the brittle deformation linked to normal faulting (T4). Joint set J2 is found near thrust Th1 (S7, S11, S18) and—within the FW ANT—closer to thrust Th2 (S1–4 and S8–10); DSE analysis of TLS point cloud features J2 as the most relevant joint set in the core of the HW ANT (Fig. 10; Table 2). This significant evidence suggests that this joint set likely developed as a consequence of thrusting (T2). The geometric combination of J2 and J1 favours wedge sliding failure mechanisms both in the FW ANT and the core of the HW ANT (Fig. 14a; Table 3). In contrast, the absence of J2 within the northern flank of the HW ANT (sites S12–17 in Fig. 9) made partially unfavourable the same kind of failure.

Therefore while wedge sliding and toppling mechanisms coexist in the FW ANT and the core of the HW ANT, toppling is prevalent in the rest of the HW ANT sector (Table 3). This last mechanism mainly develops along the joint sets related to the strike-slip event (T3), such as J6 (Fig. 14b, c) and J7 which are often counter-slope dipping.

Once failure mechanisms were acknowledged, volumes of potentially unstable rock blocks were estimated at sites S1–18 or calculated by DSE point cloud analysis at S19. From these values, different design blocks were inferred for the geological domains HW

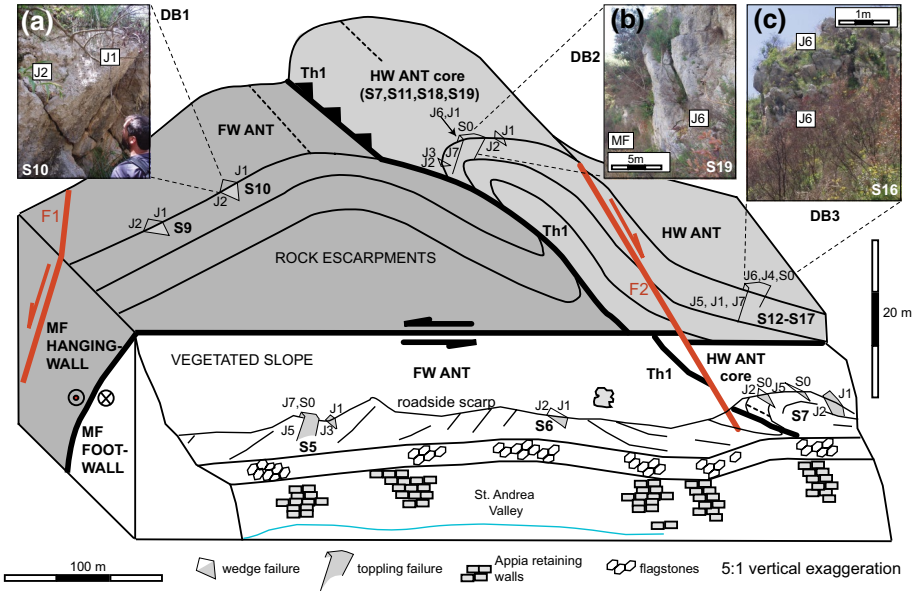

Fig. 14 Block diagram of the HW ANT and FW ANT domains highlighting the relationship between joints distribution, failure mechanisms and main structural features; **a** rock wedge geometry, **b**, **c** evidence of toppling of different sizes

ANT, HW ANT core and FW ANT, all in the order of a few cubic metres (Table 3). Before considering such an order of magnitude it was necessary to investigate the role played by a few mega-joints belonging to set J1 and having plurimetric lengths, large spacing and wide openings. Rock pillars 1 and 2 shown by UAS images in Fig. 11a are affected by a high degree of internal tectonic deformation which leads to a disruption of the rock mass (Fig. 11b, c). Therefore, it is unlike that a significant volume of rock (700–800 m^3) can detach from the slope face. A more realistic hypothesis sees smaller blocks that gradually detach from the slope edge, thus generating the half-circle or wedge-shaped detachment areas recognized in Fig. 11a–c.

Downstream of all these considerations, in the southern sector of the FW ANT domain (sites S1–S4 and S8–S10 in Fig. 9; Table 3), wedge sliding failures from the rock slope may involve rock volumes between 0.1 and 3.3 m^3, not very different from the values for events of toppling failures (0.8–3.0 m^3). Then, a first design block DB1 with a volume of 3.5 m^3 was defined and assigned to detachment areas 1–5 (Figs. 6, 15). In the central sector, near Th1 and within the core of the HW ANT (sites S7, S11, S18 and S19), the rock escarpment is 20 m high due to the morphological signature of the MF (Fig. 11a) and toppling plays an important role in possible failures (Fig. 14b). A design block DB2 of 7 m^3 was assumed for detachment areas 6–9 (Figs. 6, 15), taking into account the maximum volume estimated from the point cloud analysis at S19 (6.7 m^3). Slightly lower values were calculated again for toppling failure at site S11 (5. 8 m^3) and for wedge failures at site S19 (4.3 m^3). In the northern part of the HW ANT domain (S12–S17), wedge sliding is absent or rare and may involve a very small volume of rock blocks detaching from the slope face (0.5–1.7 m^3 in Table 3). Again, the maximum volume corresponds to the prevailing toppling mechanism, mainly acting along J6 fractures (parallel to the MF, Fig. 14c). Due to the reduced height of the tectonic-controlled escarpment along the northern tract of the MF

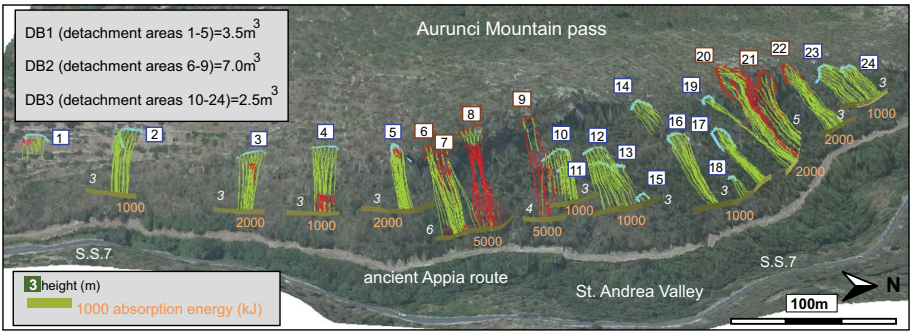

Fig. 15 3D representation of the remediation project based on positioning of rock barriers. Light (green) lines indicate rolling and sliding along slope, dark (red) lines bouncing. Sizing of countermeasures (absorption energy and height) is reported

(Fig. 3), the design block has a lower magnitude than in the HW ANT core zone, equal to 2.5 m^3 (DB3). This value was assigned to detachment areas 10–24 (Fig. 15).

The choice of maximum volumes from Table 3 may imply an overestimate of the DB volumes with respect to the bimodal distribution of fallen rock block volumes as evidenced in Fig. 12a (0.75 or 0.15 m^3). Significant fragmentation should occur during the downslope propagation, and it is reasonable to consider that a large part of this process takes place when fractured blocks reach the hard-stone pavement of the Appia route, after a rebound phase over the roadside scarp (Fig. 13b). Therefore, the volume distribution observed on the route was retained as not fully representative of the real dimensions of rock blocks potentially detaching from the main escarpment upslope. The choice for DB1–DB3 volumes identified on the rock slope edge definitively ensures a greater degree of safety of the remediation plane. In addition, the distinction of a greater value for DB1 is consistent with a higher concentration of large blocks ($0.25 < V < 1$ m^3 and $1 < V < 2$ m^3) in the central part of the route track (Fig. 8b).

Table 4 reports calculations to estimate the necessary absorption energy of the rock barrier that should be installed to protect the ancient Appia route. For each design block

Table 4 Estimate of barrier absorption energy for different design block volumes

	V (m^3)	Mass (kg)	Weight (N)	$Ecin_{max}$ (m^2/s^2)	Energy (kJ)	Barrier energy (kJ)
DB2	7	17,500	171,675	250	4375	5000
				200	3500	5000
DB1	3.5	8750	85,837.5	150	1312.5	2000
				100	875	1000
DB3	2.5	6250	61,312.5	200	1250	2000
				100	625	1000

A rock density $\delta = 2500$ kg/m^3 for the carbonate rock masses was considered

DB1–3, design blocks; $Ecin_{max}$, maximum value of specific kinetic energy observed along the slope (see Fig. 13c)

DB1–DB3, the block mass ($V{\cdot}\delta$, with $\delta = 2500$ kg/m^3) was multiplied by different values of the specific kinetic energy (m^2/s^2) (Fig. 13c). Then, the value of the absorption energy required for the rock block to be stopped was derived, ranging from 1000 to 5000 kJ. Different sizing (length, height, absorption energy) of the protection barrier was then evaluated, and its positioning was planned considering rock fall trajectories (Fig. 13b), distribution of kinetic energy and bouncing height along the slope (Fig. 13c, d).

Figure 15 illustrates the 3D representation of the remediation project aimed at reducing the local geohazard determined by rock falls along the ancient Appia route. The absorption energy and height of each barrier were differentiated according to modelling results. Rock fall barriers are positioned very close to each other and in some cases with linear overlaps; this to avoid damage by events from unexpected source areas. The project should be arranged in the next few years to ensure the protection of the archaeological site and the safe fruition by visitors. However, the same remediation plan should be integrated with continuous monitoring and an adequate early warning system.

7 Conclusion

The Mesozoic carbonate rock slope that is crossed by the ancient Appia route track at the Aurunci Mountain pass is affected by rock falls, which represent a serious danger for the preservation and fruition of the archaeological site. The same rock slope shows a morphotectonic inheritance with evidence of four tectonic phases, including Neogene folding and thrusting, undated strike-slip tectonics and Plio–Pleistocene normal faulting. Related brittle deformation includes both persistent and scattered joint sets unequally distributed over the area.

The results of field-based structural analysis and remote sensing surveys (TLS and UAS) outline how distribution of joint sets along the slope influences the type of rock failure mechanism and size of falling blocks. Low-angle joint surfaces (J2) are concentrated near compressive structural features whereas high-angle and slope-parallel discontinuities (J6) gather along a deformation zone developed near a main strike-slip fault that has a clear morphogenetic role in the local landscape. The only persistent joint system in the area (J1) can be attributed to normal faulting, it is highly oblique to the slope direction and locally features extensive and wide-open discontinuities.

As a consequence of joint spatial variations, prevailing wedge sliding and toppling failure mechanisms can involve three different design blocks, one doubling the others in volumetric terms (7 m^3, 3.5 m^3, and 2.5 m^3). Design block volumes were included in a probabilistic, kinematic modelling of the rock fall process. Model results were obtained after calibration by a back-analysis procedure and using an inventory of fallen rock blocks documented over the Appia flagstone as a main constraint. Finally, a remediation project was designed that should guarantee protection of the cultural heritage and visiting tourists through the placement of elastic barriers with absorption energy ranging between 1000 and 5000 kJ.

Acknowledgements This research was conducted in the framework of a Future In Basic Research (FIRB) project joined by the CNR and the Department of Literature and Cultural Heritage (DILBEC) of the Campania University "L. Vanvitelli". The authors are grateful to Paola Carfora from DILBEC who has made results of aero-photogrammetric modelling of the St. Andrea Valley available for this work. Thanks also go to Carlo Esposito ("Sapienza" University of Rome), Gianluca Bianchi Fasani (ENEA) and Francesco Manigrasso for their help during field surveys. On-site logistical assistance was guaranteed by the forest rangers of the Aurunci National Park. Financial funding came from MIUR—Italian Ministry for Education,

University and Research (FIRB Project RBFR10DKZK, Di Luzio E. Principal Investigator when employed at CNR-ITABC, Institute for Technologies Applied to Cultural Heritage).

Funding FIRB project RBFR10DKZK, Di Luzio E. Principal Investigator.

Code availability ROCSCIENCE Software suite (Dips, Plane, Topple, Wedge). License code: 8324A. ROTOMAP software (Geo&soft international). Hardkey code: T3N2781.

Compliance with ethical standards

Conflict of interest The authors declare that they have no conflict of interest.

Availability of data and materials Data collected in the context of the FIRB project.

References

Abellan A, Vilaplana JM, Calvet J, Blanchard J (2010) Detection and spatial prediction of rockfalls by means of terrestrial laser scanning modelling. Geomorphology 119(3–4):162–171. https://doi.org/10.1016/j.geomorph.2010.03.016

Abellan A, Oppikofer T, Jaboyedoff M, Rosser NJ, Lim M, Lato MJ (2014) Terrestrial laser scanning of rock slope instabilities. Earth Surf Process Landf 39:80–97. https://doi.org/10.1002/esp.3493

Agliardi F, Crosta GB (2003) High resolution three-dimensional numerical modeling of rockfalls. Int J Rock Mech Min Sci 40:455–471. https://doi.org/10.1016/S1365-1609(03)00021-2

Agliardi F, Crosta GB, Zanchi A (2001) Structural constraints on deep-seated slope deformation kinematics. Eng Geol 59:83–102. https://doi.org/10.1016/S0013-7952(00)00066-1

Agliardi F, Zanchi A, Crosta GB (2009) Tectonic vs gravitational morphostructures in the Central Italian Alps: constraints on the recent evolution of the mountain range. Tectonophysics 474:250–270. https://doi.org/10.1016/j.tecto.2009.02.019

Agliardi F, Crosta GB, Meloni F, Valle C, Rivolta C (2013) Structurally-controlled instability, damage and slope failure in a porphyry rock mass. Tectonophysics 605:34–47. https://doi.org/10.1016/j.tecto.2013.05.033

Aksoy H, Ercanoglu M (2006) Determination of the rockfall source in an urban settlement area by using a rule-based fuzzy evaluation. Nat Hazards Earth Syst Sci 6:941–954. https://doi.org/10.5194/nhess-6-941-2006

Ambrosi C, Crosta GB (2006) Large sackung along major tectonic features in the Central Italian Alps. Eng Geol 83:183–200. https://doi.org/10.1016/j.enggeo.2005.06.031

Azzoni A, de Freitas MH (1995) Experimentally gained parameters, decisive for rock fall analysis. Rock Mech Rock Eng 28:111–124. https://doi.org/10.1007/BF01020064

Azzoni A, La Barbera G, Zaninetti A (1995) Analysis and prediction of rockfalls using a mathematical model. Int J Rock Mech Min Sci 32:709–724. https://doi.org/10.1016/0148-9062(95)00018-C

Badger TC (2002) Fracturing within anticlines and its kinematic control on slope stability. Environ Eng Geosci 8(1):19–33. https://doi.org/10.2113/gseegeosci.8.1.19

Baleani M, Mazzanti P (2017) Analisi geostrutturale 2.0: caratterizzazione di un ammasso roccioso attraverso nuvole di punti. INGENIO 54. Retrieved April 28, 2020, https://www.ingenio-web.it/6923-analisi-geostrutturale-20caratterizzazione-di-un-ammasso-roccioso-attraverso-nuvole-di-punti

Barton N, Choubey V (1977) The shear strength of rock joints in theory and practice. Rock Mech 10:1–54. https://doi.org/10.1007/BF01261801

Bianchi Fasani G, Di Luzio E, Esposito C, Martino S, Scarascia Mugnozza G (2011) Numerical modelling of Plio-Quaternary slope evolution based on geological constraints: a case study from the Caramanico Valley (Central Apennines, Italy). Geol Soci Lond Spec Publ 351:201–214. https://doi.org/10.1144/SP351.11

Bianchi Fasani G, Di Luzio E, Esposito C, Evans SG, Scarascia Mugnozza G (2014) Quaternary, catastrophic rock avalanches in the Central Apennines (Italy): relationships with inherited tectonic features, gravity-driven deformations and the geodynamic frame. Geomorphology 211:22–42. https://doi.org/10.1016/j.geomorph.2013.12.027

Boldini D, Guido GL, Margottini C et al (2018) Stability analysis of a large-volume block in the historical rock-cut city of Vardzia (Georgia). Rock Mech Rock Eng 51:341–349. https://doi.org/10.1007/s00603-017-1299-7

Bourrier F, Lambert S, Baroth J (2015) A reliability-based approach for the design of rockfall protection fences. Rock Mech Rock Eng 48:247–259. https://doi.org/10.1007/s00603-013-0540-2

Brideau MA, Yan M, Stead D (2009) The role of tectonic damage and brittle rock fracture in the development of large rock slope failures. Geomorphology 103:30–49. https://doi.org/10.1016/j.geomorph.2008.04.010

Broili L (1973) In situ tests for the study of rockfall. Geol Appl Idrogeol 8:105–111

Bruce IG, Cruden DM, Eaton TM (1989) Use of a tilting table to determine the basic friction angle of hard rock samples. Can Geotech J 26(3):474–479. https://doi.org/10.1139/t89-060

Budetta P, Santo A (1994) Morphostructural evolution and related kinematics of rockfalls in Campania (southern Italy): a case study. Eng Geol 36:197–210. https://doi.org/10.1016/0013-7952(94)90004-3

Cavinato GP, De Celles PG (1999) Extensional basins in the tectonically bimodal Central Apennines fold-thrust belt, Italy: response to corner flow above a subducting slab in retrograde motion. Geology 27(10):955–958. https://doi.org/10.1130/0091-7613(1999)027%3c0955:EBITTB%3e2.3.CO;2

Centamore E, Di Manna P, Rossi D (2007) Kinematic evolution of the Volsci Range: a new overview. Ital J Geosci 126:159–172

Chau KT, Wong RHC, Wu JJ (2002) Coefficient of restitution and rotational motions of rockfall impacts. Int J Rock Mech Min Sci 39:69–77. https://doi.org/10.1016/S1365-1609(02)00016-3

Coe JA, Harp EL (2007) Influence of tectonic folding on rockfall susceptibility, American Fork Canyon, Utah, USA. Nat Hazards Earth Syst Sci 7:1–4. https://doi.org/10.5194/nhess-7-1-2007

Copons R, Vilaplana JM (2008) Rockfall susceptibility zoning at a large scale: from geomorphological inventory to preliminary land use planning. Eng Geol 102(3–4):142–151. https://doi.org/10.1016/j.enggeo.2008.03.020

Cosentino D, Cipollari P, Di Donato V, Sgrosso I, Sgrosso M (2002) The Volsci Range in the kinematic evolution of the northern and southern Apennine orogenic system. Ital J Geosci Spec 1:209–218

Crosta GB, Agliardi F (2004) Parametric evaluation of 3D dispersion of rockfall trajectories. Nat Hazards Earth Syst Sci 4(4):583–598

Cruden DM, Hu XQ (1988) Basic friction angles of carbonate rocks from Kananaskis country. Can Bull Int As Eng Geol 38:55–59

Cruden DM, Varnes DJ (1996) Landslide types and processes, transportation and Road Research Board, Special Report 247, National Academy of Sciences, pp 36–75

Di Luzio E (2019) Inquadramento geologico e geomorfologico. Aspetti principali e dissesto idrogeologico nell'area. In: Di Luzio E, Carfora P (eds) Approcci multidisciplinari per la ricostruzione del paesaggio di una grande strada romana. La via Appia al valico degli Aurunci. Claudio Grenzi Editore, Foggia, pp 23–36. ISBN 978-88-8431-726-1

Di Luzio E, Carfora P (2018) Geomorphological records of diachronous quarrying activities along the ancient Appia route at the Aurunci Mountain Pass (Central Italy). Geomorphology 306:210–223. https://doi.org/10.1016/j.geomorph.2018.01.016

Di Luzio E, Saroli M, Esposito C, Bianchi-Fasani G, Cavinato GP, Scarascia-Mugnozza G (2004) The influence of inherited structural framework on deep-seated gravity deformation phenomena: the fault-bounded Majella anticline (central Apennines, Italy). Geomorphology 60:417–432. https://doi.org/10.1016/j.geomorph.2003.10.004

Di Luzio E, Bianchi Fasani G, Bretschneider A (2013) Potential rockfalls and analysis of slope dynamics in the Palatine archaeological area. Geol Acta 11(2):245–264. https://doi.org/10.1344/105.000001834

Dinçer I, Orhan A, Frattini P, Crosta GB (2016) Rockfall at the heritage site of the Tatlarin Underground City (Cappadocia, Turkey). Nat Hazards 82:1075–1098. https://doi.org/10.1007/s11069-016-2234-z

Dorren L (2003) A review of rockfall mechanics and modelling approaches. Prog Phys Geogr 27(1):69–87. https://doi.org/10.1191/0309133303pp359ra

Dorren L, Seijmonsbergen A (2003) Comparison of three GIS-based models for predicting rockfall runout zones at a regional scale. Geomorphology 56:49–64. https://doi.org/10.1016/S0169-555X(03)00045-X

Esposito C, Martino S, Scarascia Mugnozza G (2007) Mountain slope deformations along thrust fronts in jointed limestone: an equivalent continuum modelling approach. Geomorphology 90(1):55–72. https://doi.org/10.1016/j.geomorph.2007.01.017

Esposito C, Di Luzio E, Scarascia Mugnozza G, Bianchi Fasani G (2014) Mutual interactions between slope-scale gravitational processes and morpho-structural evolution of central Apennines (Italy): review of some selected case histories. Rend Lincei Sci Fis Nat 25(2):155–161. https://doi.org/10.1007/s12210-014-0348-3

Evans SG, Hungr O (1993) The assessment of rockfall hazard at the base of talus slopes. Can Geotech J 30:620–636. https://doi.org/10.1139/t93-054

Fanti R, Gigli G, Lombardi L, Tapete D, Canuti P (2013) Terrestrial laser scanning for rockfall stability analysis in the cultural heritage site of Pitigliano (Italy). Landslides 10(4):409–420. https://doi.org/10.1007/s10346-012-0329-5

Ferrari F, Giani GP, Apuani T (2013) Towards the comprehension of rockfall motion, with the aid of in situ tests. Ital J Eng Geol Environ 6:163–171. https://doi.org/10.4408/IJEGE.2013-06.B-13

Fiorucci M, Marmoni G, Martino S, Mazzanti P (2018) Thermal response of jointed rock masses inferred from infrared thermographic surveying (Acuto test-site, Italy). Sensors 18:2221. https://doi.org/10.3390/s18072221

Galadini F, Messina P (2004) Early-Middle Pleistocene eastward migration of the Abruzzi Apennine (Central Italy) extensional domain. J Geodyn 37:57–81. https://doi.org/10.1016/j.jog.2003.10.002

Giani GP (1992) Rock slope stability analysis. A.A. Balkema, Rotterdam, p 374

Gigli G, Morelli S, Fornera S, Casagli N (2012) Terrestrial laser scanner and geomechanical surveys for the rapid evaluation of rock fall susceptibility scenarios. Landslides. https://doi.org/10.1007/s10346-012-0374-0

Gonzalez de Vallejo LI, Ferrer M, Ortuno L, Oteo C (2005) Geoingegneria. Pearson Education Italia. ISBN 13:978-88-7192-094-8

Goodman RE (1989) Introduction to rock mechanics, 2nd edn. Wiley, New York

Guo J, Wang J (2018) Mechanism analysis of the failure for a safe jointed rock high slope: tectonic structures and damage. Geotech Geol Eng 36(1):455–467. https://doi.org/10.1007/s10706-017-0339-0

Guzzetti F, Crosta G, Detti R, Agliardi F (2002) STONE: a computer program for the three-dimensional simulation of rock-falls. Comput Geosci 28(9):1079–1093. https://doi.org/10.1016/S0098-3004(02)00025-0

Guzzetti F, Reichenbach P, Wieczorek GF (2003) Rockfall hazard and risk assessment in the Yosemite Valley, California, USA. Nat Hazards Earth Syst Sci 3:491–503. https://doi.org/10.5194/nhess-3-491-2003

Guzzetti F, Reichenbach P, Ghigi S (2004) Rockfall hazard and risk assessment along a transportation corridor in the Nera Valley, Central Italy. Environ Manag 34:191–208. https://doi.org/10.1007/s00267-003-0021-6

Hoek E, Bray JW (1981) Rock slope engineering, 3rd edn. The Institution of Mining and Metallurgy, London

Humair F, Pedrazzini A, Epard JL, Froese CR, Jabedoyff M (2013) Structural characterization of Turtle Mountain anticline (Alberta, Canada) and impact on rock slope failure. Tectonophysics 605:133–148. https://doi.org/10.1016/j.tecto.2013.04.029

Hungr O, Leroueil S, Picarelli L (2014) The Varnes classification of landslide types, an update. Landslides 11(2):167–194. https://doi.org/10.1007/s10346-013-0436-y

ISRM (2007) The Complete ISRM Suggested Methods for Rock Characterization, Testing and Monitoring: 1974–2006. Suggested Methods Prepared by the Commission on Testing Methods, International Society for Rock Mechanics, R. Ulusay & J.A. Hudson (eds) Compilation arranged by the ISRM Turkish National Group, Ankara

Jaboyedoff M, Metzger R, Oppikofer T, Couture R, Derron MH, Locat J, Turmel D (2007) New insight techniques to analyze rock-slope relief using DEM and 3D-imaging cloud points: COLTOP-3D software. In: Eberhardt E, Stead D, Morrison T (eds) Rock mechanics: Meeting Society's Challenges and Demands, vol 1, pp 61–68

Jaboyedoff M, Oppikofer T, Abellán A, Derron MH, Loye A, Metzger R, Pedrazzini A (2012) Use of LIDAR in landslide investigations: a review. Nat Hazards 61(1):5–28. https://doi.org/10.1007/s11069-010-9634-2

Kellog KS (2001) Tectonic controls on large landslide complex: Williams Fork Mountains near Dillon, Colorado. Geomorphology 41:355–368. https://doi.org/10.1016/S0169-555X(01)00067-8

Lan H, Martin CD, Lim CH (2007) Rock fall analyst: a GIS extension for three-dimensional and spatially distributed rock fall hazard modeling. Comput Geosci 33:262–279. https://doi.org/10.1016/j.cageo.2006.05.013

Li L, Lan H (2015) Probabilistic modeling of rockfall trajectories: a review. Bull Eng Geol Environ 74:1163–1176. https://doi.org/10.1007/s10064-015-0718-9

Margottini C, Antidze N, Corominas J et al (2015) Landslide hazard, monitoring and conservation strategy for the safeguard of Vardzia Byzantine monastery complex, Georgia. Landslides 12:193–204. https://doi.org/10.1007/s10346-014-0548-z

Markland JT (1972) A useful technique for estimating the stability of rock slope when the rigid wedge sliding type of failure is expected. Rock Mechanics Research Report 19. Imperial College, London

Martino S, Mazzanti P (2014) Integrating geomechanical surveys and remote sensing for sea cliff slope stability analysis: the Mt. Pucci case study (Italy). Nat Hazards Earth Syst Sci 14:831–848. https://doi.org/10.5194/nhess-14-831-2014

Massironi M, Genevois R, Floris M, Stefani M (2011) Influence of the antiformal setting on the kinematics of a large mass movement: the Passo Vallaccia, eastern Italian Alps. Bull Eng Geol Environ 70:497–506. https://doi.org/10.1007/s10064-010-0340-9

Matasci B, Stock GM, Jaboyedoff M et al (2018) Assessing rockfall susceptibility in steep and overhanging slopes using three-dimensional analysis of failure mechanisms. Landslides 15(5):859–878. https://doi.org/10.1007/s10346-017-0911-y

Mazzanti P, Schilirò L, Martino S, Antonielli B, Brizi E, Brunetti A, Margottini C, Scarascia Mugnozza G (2018) The contribution of terrestrial laser scanning to the analysis of cliff slope stability in Sugano (Central Italy). Remote Sens 10(9):1475. https://doi.org/10.3390/rs10091475

Niethammer U, James MR, Rothmund S, Travelletti J, Joswig M (2012) UAV-based remote sensing of the Super-Sauze landslide: evaluation and results. Eng Geol 128:2–11. https://doi.org/10.1016/j.enggeo.2011.03.012

Pantelidis L, Kokkalis A (2011) Designing passive rockfall measures based on computer simulation and field experience to enhance highway safety. Int J Rock Mech Min Sci 48:1369–1375. https://doi.org/10.1016/j.ijrmms.2011.09.008

Parotto M, Tallini M (2013) Geometry and kinematics of the Montelanico-Carpineto backthrust (Lepini Mts., Latium) in the hangingwall of the early Messinian thrust front of the central Apennines: implications for the Apennine chain building. Ital J Geosci 132(2):274–289. https://doi.org/10.3301/IJG.2012.34

Patacca E, Scandone P, Di Luzio E, Cavinato GP, Parotto M (2008). Structural architecture of the central Apennines. Interpretation of the CROP 11 seismic profile from the Adriatic coast to the orographic divide. Tectonics 27:TC3006. https://doi.org/10.1029/2005TC001917

Pedrazzini A, Jaboyedoff M, Froese CR, Moreno F, Langenberg W (2011) Structural analysis of Turtle Mountain: origin and influence of fractures in the development of rock slope failures. Geol Soc Lond Spec Publ 351(1):163–183. https://doi.org/10.1144/SP351.9

Penna IM, Abellán A, Humair F, Jaboyedoff M, Daicz S, Fauqué L (2017) The role of tectonic deformation on rock avalanche occurrence in the Pampeanas Ranges, Argentina. Geomorphology 289:18–26. https://doi.org/10.1016/j.geomorph.2016.07.006

Pfeiffer TJ, Bowen TD (1989) Computer simulation of rockfalls. Bull As Eng Geol 26:135–146. https://doi.org/10.2113/gseegeosci.xxvi.1.135

Pfeiffer TJ, Higgins JD (1990) Rockfall hazard analysis using the Colorado rockfall simulation program. Transp Res Rec 1288:117–126

Piteau DR, Clayton R (1987) Computer rockfall model. In: ISMES (ed) Proceedings of meeting on rockfall dynamics and protective works effectiveness, Bergamo, pp 123–125

Quilici L (1999) La via Appia attraverso la gola di Itri. In: Quilici L, Quilici-Gigli S (eds) Campagna e paesaggio nell'Italia antica. Atlante Tematico di Topografia Antica 8:51-94. L'Erma di Bretschneider, Rome. ISBN: 978-88-913-0146-8

Quilici L. (2004) Santuari, ville e mausolei sul percorso della via Appia al valico degli Aurunci. In: Quilici L, Quilici-Gigli S (eds) Viabilità e insediamenti nell'Italia antica. Atlante Tematico di Topografia Antica 13:441-543. L'Erma di Bretschneider, Rome. ISBN: 978-88-913-1460-4

Quilici L (2011) Il Parco della Via Appia nella valle di Sant'Andrea tra Fondi e Itri. Scavi e restauri 2006–2010. In: Quilici L, Quilici-Gigli S (eds) Atlante Tematico di Topografia Antica, vol 21, pp 81–102. L'Erma di Bretschneider. ISBN: 978-88-913-0145-1

Riquelme AJ, Abellán A, Tomás R, Jaboyedoff M (2014) A new approach for semi-automatic rock mass joints recognition from 3D point clouds. Comput Geosci 68:38–52. https://doi.org/10.1016/j.cageo.2014.03.014

Ritchie AM (1963) Evaluation of rockfall and its control. Highw Res Board Rec 17:13–28

ROCSCIENCE Software suite (Dips, Plane, Topple, Wedge). License code: 8324A

ROTOMAP by Geo&soft international. Hardkey code: T3N2781

Saintot A, Henderson IHC, Derron MH (2011) Inheritance of ductile and brittle structures in the development of large rock slope instabilities: examples from western Norway. Geol Soc Lond Spec Publ 351:27–78. https://doi.org/10.1144/SP351.3

Scarascia-Mugnozza G, Bianchi-Fasani G, Esposito C, Martino S, Saroli M, Di Luzio E, Evans SG (2006) Rock avalanche and mountain slope deformation in a convex, dip-slope: the case of the Majella Massif (central Italy). In: Evans SG, Scarascia-Mugnozza G, Ermanns R, Strom A (eds) Massive rock slope failure, Nato Science Series Book. Kluwer, Dordrecht, pp 357–376. ISBN 978-1-4020-4037-5

Scioldo G (1991) Rotomap: analisi statistica del rotolamento dei massi. In: Guariso G (ed) Guida di informatica ambientale. Patron, Bologna, pp 81–84
Scioldo G (2006) User guide: ISOMAP & ROTOMAP—3D surface modelling and rockfall analysis. Retrieved April 28, 2020, http://www.geoandsoft.com/english/download.htm
Stead D, Wolter A (2015) Critical review of rock slope failure mechanisms: the importance of structural geology. J Struct Geol 74:1–23. https://doi.org/10.1016/j.jsg.2015.02.002
Sturzenegger M, Stead D (2009) Quantifying discontinuity orientation and persistence on high mountain rock slopes and large landslides using terrestrial remote sensing techniques. Nat Hazards Earth Syst Sci 9:267–287. https://doi.org/10.5194/nhess-9-267-2009
Sturzenegger M, Stead D, Elmo D (2011) Terrestrial remote sensing-based estimation of mean trace length trace intensity and block size/shape. Eng Geol 119(3–4):11–96. https://doi.org/10.1016/j.enggeo.2011.02.005
Trigila A (2007) Rapporto sulle frane in Italia—Il Progetto IFFI: metodologia, risultati e rapporti regionali (Rapporti APAT 78/2007). ISBN:978-88-448-0310-0
Trigila A, Iadanza C. (2008) Landslides in Italy. Special report 2008 (Rapporti ISPRA 83)
Tunusluoglu MC, Zorlu K (2009) Rockfall hazard assessment in a cultural and natural heritage (Ortahisar Castle, Cappadocia, Turkey). Environ Geol 56(5):963–972. https://doi.org/10.1007/s00254-008-1198-z
Vangeon JM, Hantz D, Dussauge C (2001) Rockfall predictibility: a probabilistic approach combining historical and geomechanical studies. Rev Francaise de Geotech 95(96):143–154
Varnes DJ (1978) Slope movement types and processes. In: Schuster RL, Krizek RJ (eds) Landslides, analysis and control, special report 176. Transportation research board, National Academy of Sciences, Washington, pp 11–33
Waltham AC (2009) Foundations of engineering geology, 3rd edn. Spon Press, Tayòlor and Francis, London
Wang X, Zhang L, Wang S et al (2012) Field investigation and rockfall hazard zonation at the Shijing Mountains Sutra caves cultural heritage (China). Environ Earth Sci 66:1897–1908. https://doi.org/10.1007/s12665-011-1414-0
Wieczorek GF, Stock GM, Reichenbach P, Snyder JB et al (2008) Investigation and hazard assessment of the 2003 and 2007 Staircase Falls rock falls, Yosemite National Park, California, USA. Nat Hazards Earth Syst Sci 8(3):421–432

Affiliations

E. Di Luzio[1] · P. Mazzanti[2] · A. Brunetti[2] · M. Baleani[2]

P. Mazzanti
paolo.mazzanti@nhazca.com

A. Brunetti
alessandro.brunetti@nhazca.com

M. Baleani
marco.baleani@nhazca.com

[1] CNR-IGAG, Consiglio Nazionale delle Ricerche (National Research Council), Istituto di Geologia Ambientale e Geoingegneria (Institute of Environmental Geology and Geoengineering), Area della Ricerca RM1 - Montelibretti, Via Salaria Km 29.3, Monterotondo St., 00165 Rome, Italy

[2] NHAZCA s.r.l., Spin-off "Sapienza" University of Rome, Via Vittorio Bachelet, 12, 00185 Rome, Italy